Biophysical Journal, Volume 97

Supporting Material

High-chloride concentrations abolish the binding of adenine nucleotides in the mitochondrial ADP/ATP carrier family

Eva-Maria Krammer , Stéphanie Ravaud , François Dehez , Annie Frelet-Barrand , Eva Pebay-Peyroula , and Christophe Chipot

High–chloride concentrations abolish the binding of adenine nucleotides in the mitochondrial ADP/ATP carrier family

Eva-Maria Krammer*, Stéphanie Ravaud†, François Dehez*, Annie Frelet-Barrand‡, Eva Pebay-Peyroula† and Christophe Chipot*¶

* Equipe de dynamique des assemblages membranaires, UMR No. 7565 CNRS-UHP, Nancy Université, BP 239, 54506 Vandœuvre-lès-Nancy cedex, France, † Institut de biologie structurale, UMR No. 5075 CEA-CNRS-UJF, Grenoble Université, 41, rue Jules Horowitz, 38027 Grenoble cedex 1, France and ‡Laboratoire de Physiologie Cellulaire Végétale, CNRS (UMR-5168)/CEA/INRA (UMR-1200)/UJF, CEA, DSV, iRTSV, 17 rue des Martyrs 38054 Grenoble Cedex 9, France;¶ Current address: Theoretical and Computational Biophysics Group, Beckman Institute, University of Illinois at Urbana-Champaign, 405 North Mathews, Urbana, Illinois 61801

Supporting Information

Transport measurements on intact E. coli *cells*

DNA construct and heterologous expression of AAC in E. coli. The *Arabidopsis thaliana* ADP/ATP carrier 1 (AtAAC1) gene was cloned without the mitochondrial transit sequence corresponding to the first 63 residues [1]. The resulting cDNA coding for the mature form of AtAAC1 was amplified by PCR with the Phusion High Fidelity DNA polymerase (Finnzymes, Finland) from an *Arabidopsis thaliana* cDNA library using the following primers: AAC1-TOPO forward *CACC***ATG**GCTTCTCCCGTGTTTGTCCAAACC and AAC1-TOPO reverse **CTA***CTTCTCGAATTGTGGGTGTGACCA*GG CACCTCCTGATCCGTACTTCTT (the italics corresponds to a *Strep*-tag II, the start and stop codon are indicated in bold and the sequence of the cDNA is underlined). The PCR product was inserted into the entry vector pENTR-D-Topo, further transferred to the expression vector pDEST-17 by LR reaction (Invitrogen) and checked by sequencing. The nucleotide sequence of AtAAC1 is available under the accession numbers: At3g08580 (Arabidopsis Genome Initiative database) or P31167 (TrEMBL database). AtAAC1 (or control expression plasmid pET20b) were expressed in the *E. coli* cells C43 (DE3). Transformed *E. coli* cells were inoculated with a fresh overnight culture and grown at 37°C in LB medium [2]. Although the unfavorable codon usage of *E. coli* was anticipated to hamper expression of the carriers, leading to protein production in inclusion bodies [3, 4], AtAAC1 was expressed without significant retardation of *E. coli* cell growth. Protein expression was induced at an optical density (OD600) of 0.6-0.8 by the addition of 0.1 mM IPTG. Cells were grown overnight at 20°C and collected by centrifugation for 10 min at 5000 g. The pellets were resuspended in potassium phosphate buffer (50 mM, pH 7.0) to a final concentration of 100 μg μL^{-1}.

Uptake of radioactively labeled ATP. On account of the "positive–inside" rule, the N– and C–termini of AtAAC1 are probably located in the periplasm, hence orienting the CATR-cavity outwards [7, 8]. Uptake experiments were carried out according to Haferkamp *et al.* (2002), Tjaden *et al.* (1998) and Thuswaldner *et al.* (2007) with a few modifications [2, 5, 6]. IPTG-induced *E. coli* cells (30 μ L, 100 μg μL^{-1}) were incubated in 50 mM potassium phosphate buffer (pH 7.0) containing 50 μM [α-^{32}P]ATP (3000 mCi/mmol; Perkin Elmer) at 25°C for indicated time periods. Uptake of nucleotides was quenched by addition of 1 mL of ice-cold potassium phosphate buffer [9, 10]. Subsequently, the cells were filtrated through a 0.45 μm filter (Millipore, France) under vacuum and washed three times with 1-mL ice-cold potassium phosphate buffer. The radioactivity retained on the filters was quantified in 3.5 mL of water in a Multi-Purpose Scintillation Counter (Beckman Coulter, Fullerton, USA). To assess the effect of NaCl on the [α-^{32}P]ATP uptake by AtAAC1, cells were preincubated with either 0 M, 0.15 M, 0.5 M or 0.6 M NaCl. In Figure 1 in the main text, the control nucleotide uptake (control plasmid) in presence of NaCl was subtracted and the transport rate in the absence of NaCl was set to 100 %.

Molecular-dynamics simulations of bovine-heart AAC

Molecular assays. Three distinct assays were used to model AAC in its *apo*-form in a realistic environment with different chloride concentrations in solution. For the initial conformation of the AAC, the PDB structure 1OKC [11] was used after removal of the inhibitor CATR bound to the crystal structure. Since the N– and C–terminal residues are not resolved in the crystal structure, the first residue was acetylated and the last residue amidated. The AAC was inserted in a thermalized, fully hydrated palmitoyloleylphosphatidylcholine (POPC) bilayer consisting of 228 lipid units in equilibrium with an aqueous phase formed by 9559 water molecules. The net excess charge of the *apo*-AAC was counter-balanced by adding 17 chloride counter ions. This corresponds to a chloride concentration of 0.1 M. An excess of NaCl was added to the previous system resulting in the second assay with a chloride concentration of 0.15 M. After equilibration of the 0.15 M NaCl assay, the salt concentration was further increased to 0.6 M, thus, forming the third assay.

For all three assays, the equilibrated cells have roughly the a dimension of $88 \times 81 \times 80$ Å^3. The two systems, *viz.* 0.1 M and 0.15 M NaCl assays, are representative of AAC in low-salt conditions, whereas the 0.6 M NaCl assay models a high-concentration condition.

Molecular-dynamics simulations. All MD simulations were performed in the isothermal-isobaric ensembles using the program NAMD [12]. The AAC and its environment were described by the all-atom CHARMM27 force field [13, 14] and revision thereof for lipids [15]. For the protein, CMAP corrections were introduced [16]. For the computation of long-range electrostatic interactions, the particle-mesh Ewald method [18] was used. Short-range electrostatics and Lennard-Jones interactions were smoothly truncated. The equation of motions were integrated with a time step of 2 and 4 fs for short– and long-range forces, respectively, using the Verlet I r-RESPA multiple time-step propagator [19]. Covalent bonds involving hydrogen atoms were constrained to their equilibrium length by means of the Rattle algorithm [20]. To equilibrate the 0.1 M and the 0.15 M NaCl assays fully, the system was first simulated for 60 ns with the protein frozen, 40/30 ns (0.1 M/0.15 M NaCl assay) with the backbone of the protein being held fixed and the side chain flexible, and finally 20 ns (for both assays) with the protein fully flexible. For the 0.6 M NaCl assay, the system was equilibrated after changing the NaCl concentration from 0.15 M to 0.6 M over an additional 2 ns. After equilibration, 30–ns trajectories were produced for each assay under constant-area conditions.

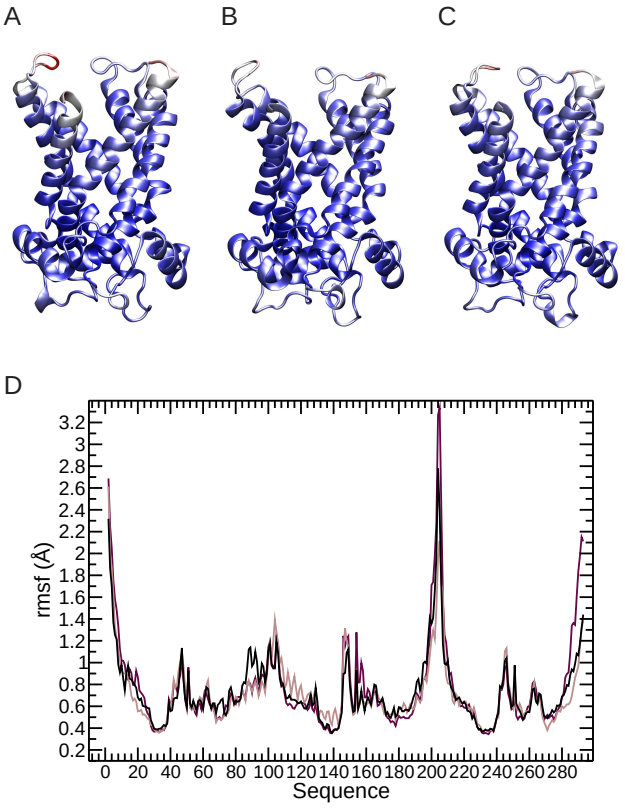

FIGURE 1 The root-mean-square fluctuations (RMSF) of the AAC does not depend on the applied chloride concentration. The RMSF is mapped on the secondary structure of the AAC for the 0.1 M (A), 0.15 M (B), and 0.6 M NaCl (C) simulation. Fluctuations range from 0.33 (blue) to 3.33 Å (red). The pictures are prepared with VMD [21]. The averaged backbone RMSF is plotted on a per residue basis (D) for the 0.1 M (dark), the 0.15 M (light) and the 0.6 M (black) assays.

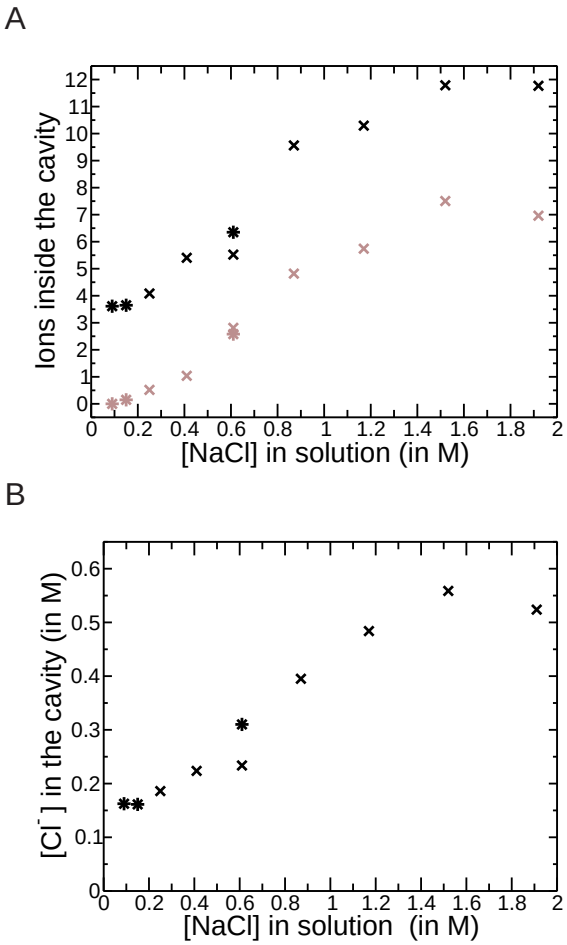

FIGURE 2 The number of chloride ions inside the cavity increases with the NaCl concentration. (A) The number of chloride (black symbols) and sodium (light symbols) is depicted as a function of the NaCl concentration. Results from long simulations (30 ns simulation time; 0.1 M, 0.15 M, and 0.6 M NaCl assay) and from short simulations (4 ns simulation time; 0.25 M, 0.41 M, 0.61 M, 0.87 M, 1.17 M, 1.52 M, and 1.91 M NaCl) are shown as stars and crosses, respectively. (B) The local chloride concentration inside the cavity is shown as a function of the NaCl concentration.

Structural deviations and fluctuations. For the 30 ns trajectory of the 0.1 M, 0.15 M, and 0.6 M NaCl assays, the time-averaged backbone distance root-mean-square deviation RMSD) from the X-ray diffraction structure (1OKC) [11] is 1.5, 1.4, and 1.6 Å, respectively (with a standard deviation of 0.14, 0.13 and 0.15 Å respectively).

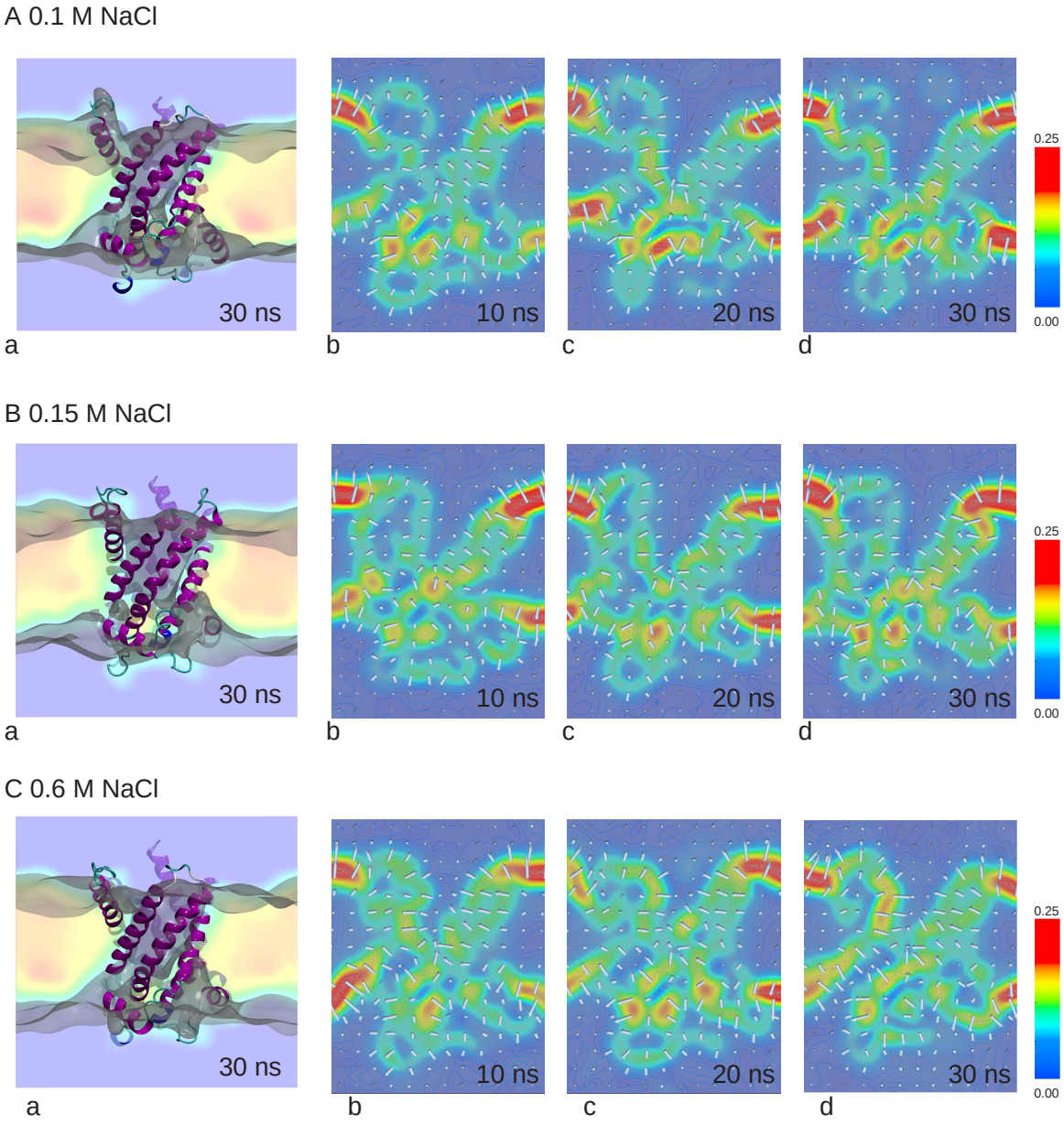

FIGURE 3 Change in the electric properties of *apo*-AAC as a function of the chloride concentration: of (A) 0.1 M NaCl, (B) 0.15 M NaCl, (C) 0.6 M NaCl. For each assay, the three-dimensional electrostatic isopotential map is shown after 30 ns of simulation time in (a). The protein and the cross-sectional view of the electrostatic potential (a) are also displayed. The cross-section of the three-dimensional map of the electric field is shown after 10 ns (b), 20 ns (c), and 30 ns (d). In all figures (b-d), the protein is oriented as in (a). The average number of chloride ions inside the cavity is 3.62/3.67/3.10 (10/20/30 ns) for the 0.1 M, 3.98/2.98/3.87 (10/20/30 ns) for the 0.15 M and 6.92/7.27/8.08 (10/20/30 ns) for the 0.6 M NaCl assays.

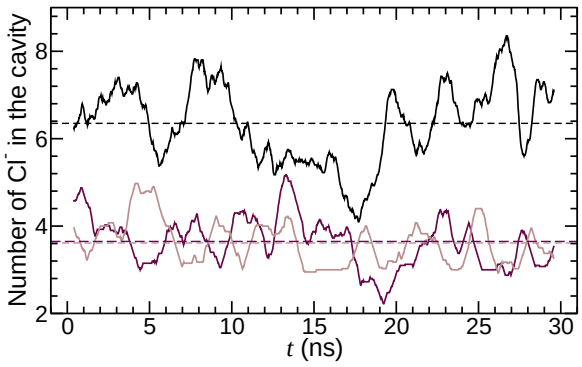

FIGURE 4 Number of chloride ions residing inside the cavity as a function of time differs between the two low– (0.1 M NaCl=dark line, 0.15 M NaCl=light line) and high–salt concentration assays (0.6 M NaCl=black line). The average number of chloride ions in the cavity, respectively 3.61/3.65/6.35 for the 0.1 M/0.15 M/0.6 M NaCl concentrations, 5 is depicted for each assay (dashed lines).

The RMSD of the 0.1 M NaCl system is lower than in previous studies of *apo*-AAC [22, 23, 24], which likely stems from different equilibration strategies. The calculated atom-wise root mean-square fluctuations (RMSF), similar for the three assays (see Figure 1), further illustrate the relative rigidity of the protein along the MD trajectories.

Mapping electric properties. The three-dimensional maps of the electrostatic potential were generated for the different assays by solving numerically the Poisson equation with the PMEPot [25] module of VMD [21]. The electric potential was averaged over 200 ps segments taken at 10 ns, 20 ns, and 30 ns of the three different MD simulations (Figure 3). The electric field was derived from the electrostatic potential using OpenDX (http://www.opendx.org), an open-source visualization software package.

Number of chloride ions close to the basic patches. The number of chloride ions near the basic residues of the upper and the lower patches differs as a function of the salt concentration (see Figure 5). In average 3.6 and 6.3 chloride ions are bound in two low–salt and the high–salt simulation (see Figure 4).

Residence time of individual chloride ions. For both low–salt simulations, the residence times of each individual chloride ion are consistent with our previous study [22]. Irrespective of the salt concentration, at least four chloride ions (Figure 6 and 7) have a residence time of more than 10 ns inside the cavity. These chloride ions interact with the residues of the lower basic patch. In the 0.6 M NaCl assay, a fifth chloride ion is monitored over 29.5 ns (Figure 7), complexed to residue R234 of the lower basic patch.

The number of ions inside the cavity is concentration dependent. The number of chloride ions inside the cavity and,

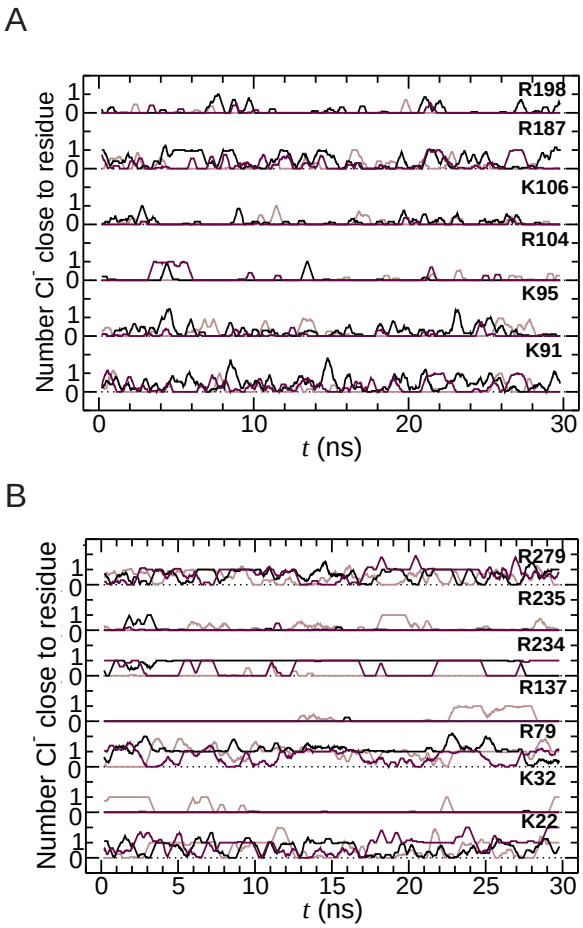

FIGURE 5 The number of chloride ions near the basic residues of the upper (A) and the lower patches (B) as a function of time differs also between the two low– (0.1 M NaCl=dark line, 0.15 M NaCl light line) and high–salt concentration (0.6 M NaCl=black line) assays.

hence, the local chloride concentration increases, starting from an NaCl solution at 0.2 M (see Figure 2). Interestingly enough, this corresponds to a situation where ADP^{3-} transport is completely abolished [26]. A few sodium ions are shown to enter also the cavity. These ions are, however, located at the top of the cavity and do not appear to participate in the inhibition process.

The binding of ADP^{3-} depends on the chloride concentration. At 0.15 M NaCl, ADP^{3-} binds to residues of the upper basic patch (see Table 1 and Figure 8) in two of the three association assays. The association processes observed here are consistent with the earlier study of Dehez *et al.* [22]. In a series of nine ligand–association assays at 0.6 M NaCl, ADP^{3-} remains unbound (see Table 1 and Figure 9). In six of these experiments, ADP^{3-} does not enter the AAC cavity (see Figure 9C, D-H), whereas in the other three experiments, the nucleotide migrates into the cavity. Yet, the position of ADP^{3-} differs significantly from the earlier observed productive binding modes [22].

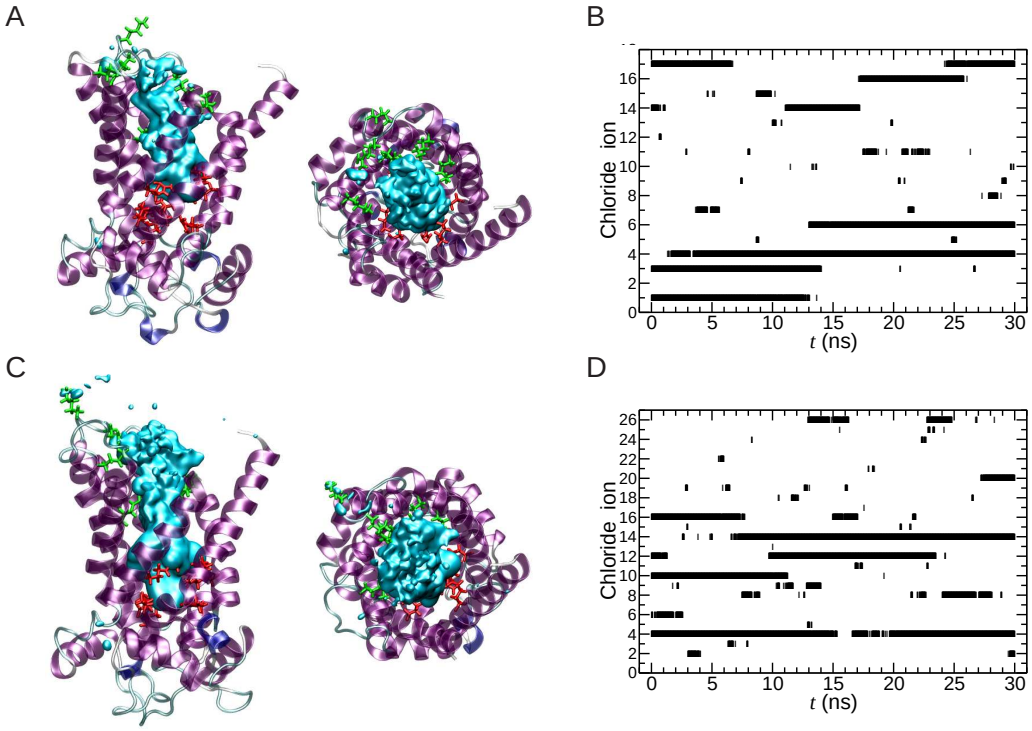

FIGURE 6 The mass-weighted isodensity map of chloride ions in the cavity of *apo*-AAC averaged over the 30 ns trajectory illuminates the portion of space occupied by chloride ions in the the 0.1 M (A) and the 0.15 M NaCl (C) assay. The upper and lower basic patches are also displayed, together with the residence time of those chloride ions found in the cavity of *apo*–AAC for the 0.1 M (B) and for the 0.15 M NaCl (D) assays.

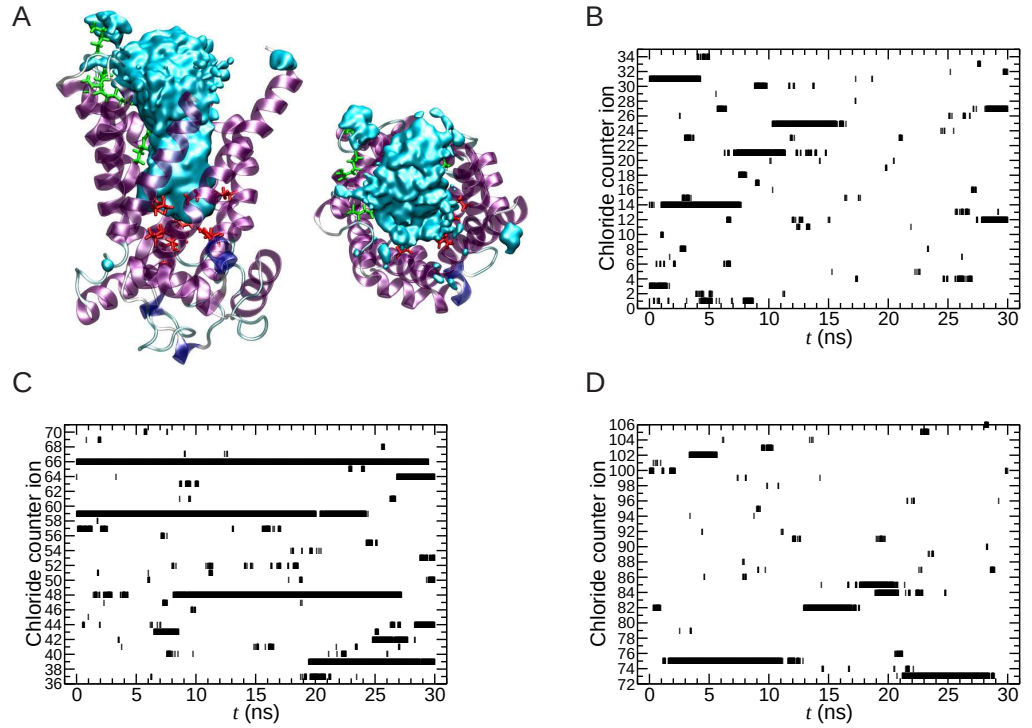

FIGURE 7 Mass-weighted isodensity map of chloride ions in the cavity of *apo*-AAC averaged over the 30 ns trajectory illuminates the portion of space occupied by chloride ions in the 0.6 M assay (A). The upper and lower basic patches are also displayed, together with the residence time of those chloride ions found in the cavity of *apo*–AAC for the 0.6 M assay. Only those ions with the number 1 to 35 (B), 36 to 71 (C), and 72 to 106 (D) are shown.

NaCl	Setup	Orientation of ADP	t	Association after t
0.15 M	A	Phosphate moiety down	20 ns	0.2 ns (K95)
0.15 M	B	Phosphate moiety down	10 ns	-
0.15 M	C	Phosphate moiety down	30 ns	0.3 ns (K95)
0.6 M	A	phosphate moiety down	40 ns	-
0.6 M	B	adenosine moiety down	40 ns	-
0.6 M	C	adenosine moiety down	40 ns	-
0.6 M	D	both moieties down	40 ns	-
0.6 M	E	both moieties down	30 ns	-
0.6 M	F	phosphate moiety down	30 ns	-
0.6 M	G	in plane	30 ns	-
0.6 M	H	in plane	30 ns	-
0.6 M	I	in plane	30 ns	-
0.1 M*	A	phosphate moiety down	10 ns	2.1 ns (K95)
0.1 M*	B	adenosine moiety down	10 ns	0.4 ns (K95)
0.1 M*	C	adenosine moiety down	10 ns	2.2 ns (K91/K95)
0.1 M*	D	both moieties down	20 ns	1.2 ns (Y194)
0.1 M*	E	both moieties down	10 ns	0.1 ns (K91)
0.1 M*	F	phosphate moiety down	10 ns	0.1 ns (K95)
0.1 M*	G	in plane	20 ns	0.9 ns (R187)
0.1 M*	H	in plane	20 ns	2.7 ns (R104)
0.1 M*	I	in plane	20 ns	0.5 ns (Y190)

Table 1 Overview of all ligand-association assays at 0.15 M and 0.6 M NaCl. For the assays at 0.6 M NaCl, the association experiment is repeated without ionic concentration (marked by *). A association event is counted whenever the substrate interacts with a basic patch residues lining the internal cavity of the carrier.

patch	a.a.	occupancy			conserv.	alternate a.a.
		0.1 M	0.15 M	0.6 M		
upper	K91	27	10	40	100	
	K95	5	15	25	96	R (3), Q(1)
	R187	21	13	43	99	P (1)
	K198	2	3	12	81	R (18), N (1)
lower	K22*	72	50	57	97	
	R79	63	78	92	99	S (1)
	R137	0	24	0	100	
	R234	52	2	87	99	S (1)
	R235	1	19	5	99	S (1)
	R279*	67	49	61	95	N (1), P (1), S (1)

* multiple-sequence alignment shows gaps at these positions.

Table 2 List of basic amino-acid (a.a.) residues interacting with the chloride ions. The percentile occupancy is defined as the fraction of time in the 30 ns simulations during which the amino acid intimately interacts with a halide ion. Percentile conservation (conserv.) and nature of the alternate amino acid occupying the same position are extracted from the MSA.

In the case example of experiment B (see Figure 10), the diphosphate moiety of ADP^{3-} interacts with K95 (after 0.9 ns), followed by binding to K91 (after 3.2 ns). The adenosine moiety is, however, not oriented towards the tyrosine ladder, but towards Q84. ADP^{3-}, therefore, appears to not be properly positioned with respect to the tyrosine ladder, which is a prerequisite for ADP^{3-} binding to and transport by the AAC.

Moreover, migration of ADP^{3-} does not lead to the exclusion of a single or several chloride ions (Figure10). The same nine ligand–association assays have been repeated without an ionic concentration, while keeping the same initial position of the substrate. All these assays resulted in productive ADP^{3-} association (see Table 1). In two experiments ADP^{3-} even binds to residues of the lower basic patch (see Figure 9).

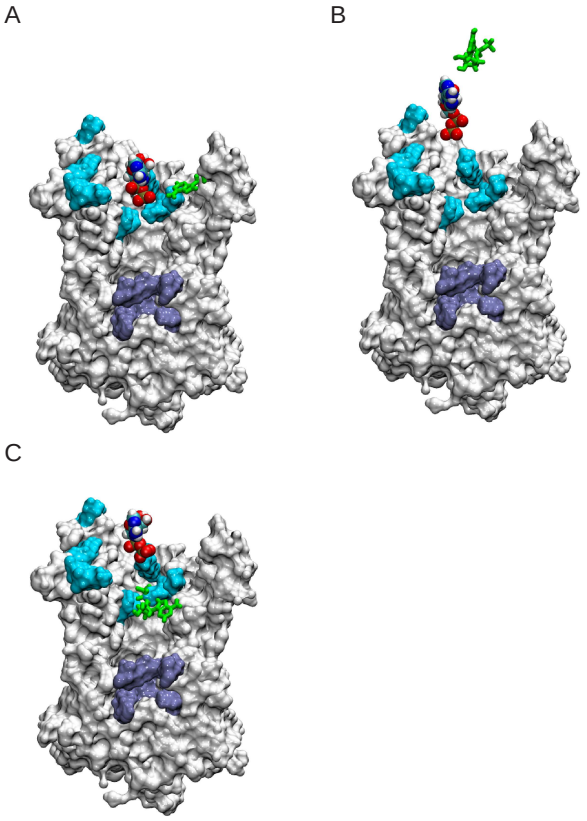

FIGURE 8 The series of three ligand-association assays leads to partial association of ADP^{3-} in presence of 0.15 M NaCl. In the setups A and C (A,C) ADP^{3-} binds to the upper basic patch whereas no binding (B) is observed in setup B. The starting and the final position of ADP^{3-} are represented as colored van der Waals spheres and as orange tubes. For the protein (white), the upper (light-blue) and lower patch (ice-blue), a molecular-surface rendering is used.

Conservation analysis of the basic patch residues in the AAC family

Multiple-sequence alignment. Starting from the sequence of the bovine-heart AAC isoform 1 (bAAC1), homologous sequences were searched using the BLAST [27] algorithm on the NCBI webpage [28]. Multiple entries of the same species, as well as sequences of hypothetical or predicted proteins were removed, and different isoforms of the same species were kept. A total of 74 sequences were considered, including the bAAC1 and AtAAC1. The origin of these sequences is listed in Table 3. All sequences carry the MCF and AAC motifs — PX(D/E)XX(K/R) and RRRMMM, respectively. No variations of the MCF motif have been witnessed in these sequences, but the AAC motif was slightly altered in six sequences (RRRLMM and SSRMMM in four and one species, respectively). These sequences were, nevertheless, kept. To obtain the multiple-sequence alignment (MSA), the 74 AAC sequences were aligned using ClustalW2 [29]. The resulting conservation analysis is summarized in Table 2.

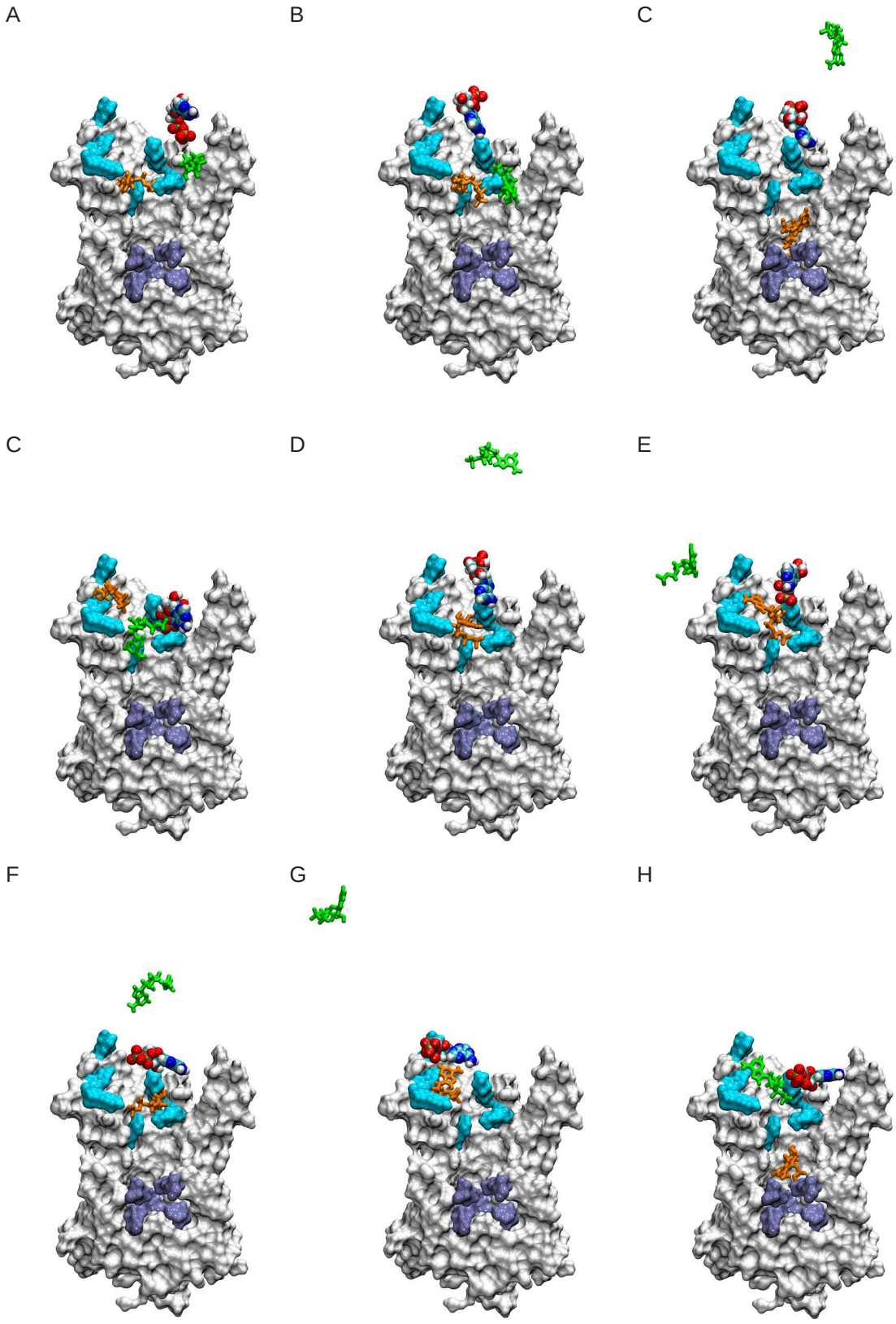

FIGURE 9 **The series of nine ligand-association assays at 0.6 M NaCl does only lead to association of the ADP^{3-} after removal of the ionic concentration. The starting position of ADP^{3-} is shown in colored van der Waals spheres. The final positions of ADP^{3-} in the presence and absence of 0.6 M NaCl are shown in green and orange tubes. For the protein (white), the upper (light-blue) and lower patch (ice-blue), a molecular-surface rendering is used.**

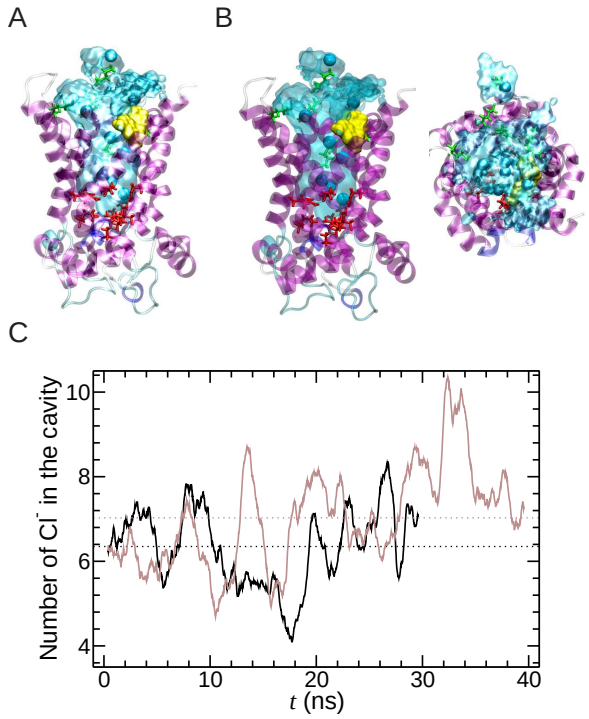

FIGURE 10 In the illustrative ligand–association assay B, no productive association is achieved, even when ADP^{3-} migrates into the cavity. (A) Final position of ADP^{3-} is shown. Residues of the upper (green), lower patch (red), and tyrosine ladder (cyan) are depicted as tubes. ADP^{3-} (yellow) and chloride ions (cyan) are shown in molecular surface and van der Waals sphere representations. (B) The mass-weighted isodensity map of the chloride ions remains unchanged. (C) The number of chloride ions inside the cavity does not decrease in association assay B (light line) compared to the 0.6 M NaCl simulation (black line).

The basic patch residues are conserved in bovine-heart and Arabidopsis thaliana AAC. The bAAC1 and AtAAC1 (mature form) sequences share 49 % sequence identity and about 74 % of sequence homology. Most of the residues lying in the CATR-cavity are conserved as shown in Figure 11. In particular, all the residues of the two basic patches are conserved in AtAAC1 (with the exception of R106).

REFERENCES and FOOTNOTES

1. Heazlewood, J. L., K. A. Howell, J. Whelan, and A. H. Millar. 2003. *Plant Physiol*, 132:230–242.
2. Haferkamp, I., J. H. Hackstein, F. G. Voncken, G. Schmit, and J. Tjaden. 2002. *Eur. J. Biochem.* 269:3172–3181.
3. Fiermonte, G., J. E. Walker, and F. Palmieri. 1993. *Biochem. J.* 294:293–299.
4. Heimpel, S., G. Basset, S. Odoy, and M. Klingenberg. 2001. *J. Biol. Chem.* 276:11499–11506.
5. Tjaden, J., C. Schwöppe, T. Möhlmann, P. W. Quick, and H. E. Neuhaus. 1998. *J. Biol. Chem.* 273:9630–9636.
6. Thuswaldner, S., J. O. Lagerstedt, M. Rojas-Stütz, K. Bouhidel, D. C. N. Leborgne-Castel, A. Mishra, F. Marty, B. Schoefs, T. Adamska, B. L. Persson,and C. Spetea. 2007. *J. Biol. Chem.* 282:8848–8859.
7. von Heijne, G. 1992. *J. Mol. Biol.* 225:487–494.
8. Bernsel, A., H. Viklund, J. Falk, E. Lindahl, G. von Heijne, and A. Elofsson, 2008. *Proc. Natl. Acad. Sci. U S A* 105:7177–7181.
9. van der Giezen M., D. J. Slotboom, D. S. Horner, P. L. Dyal, M. Harding, G. P. Xue, T. M. Embley, and E. R. Kunji. 2002. *EMBO J.* 21:572–579.
10. Monné, M., A. J. Robinson, C. Boes, M. E. Harbour, I. M. Fearnley, and E. R. Kunji. 2007. *J. Virol.* 81:3181–3186.
11. Pebay-Peyroula, E., C Dahout-Gonzalez, R. Kahn, V. Trézéguet, G. J. Lauquin, and G. Brandolin. 2003. *Nature* 426:39–44.
12. Philipps, J. C., R. Braun, W. Wang, J. Gumbart, E. Tajkhorshid, E. Villa, C. Chipot, R. D. Skeel, L. Kale, and K. Schulten. 2005. *J. Comp. Chem.* 26:1781–1782.
13. MacKerell Jr., A. D., D. Bashford, M. Bellott, R. L. Dunbrack, J. D. Evanseck, M. J. Field, S. Fischer, J. Goa, H. Guo, S. Ha, D. Joseph-McCarthy , L. Kuchnir, K. Kuczera, F. T. K. Lau, C. Mattos, S. Michnick, T. Ngo, D. T. Nguyen, B. Prodhom, W. E. Reiher, B. Roux, M. Schlenkrich, J. C. Smith, R. Stote, J. Straub, M. Watanabe, J. Wiórkiewicz-Kuczera, D. Yin, and M. Karplus. 1998. *J. Phys. Chem. B* 102:3586–3616.
14. Feller, S. E., and A. D. MacKerell Jr.. 2000. *J. Phys. Chem. B* 104:7510–7515.
15. Hénin, J., W. Shinoda, and M. L. Klein. 2008. *J. Phys. Chem.* 112:7008–7015.
16. MacKerell Jr., A. D., M. W. Feig, and C. L. Brooks. 2004. *J. Comput. Chem.* 25:1400–1415.
17. Feller, S. E., Y. Zhang, R. W. Pastor,and B. R. Brooks. 1995. *J. Chem. Phys.* 103:4613–4621.
18. Darden, T., D. York, and L. Pederson. 1993. *J. Chem. Phys.* 98:10089–10092.
19. Tuckerman, M., B. J. Berne, and G. J. Martyna. 1992. *J. Chem. Phys.* 97:1990–1999.
20. Andersen, H. C. 1983. *J. Comput. Phys.* 52:24–34.
21. Humphrey, W., A. Dalke, and K. Schulten. 1996. *J. Mol. Graph.* 14:33–38.
22. Dehez, F., and E. Pebay-Peyroula, and C. Chipot. 2008. *J. Am. Chem. Soc.* 24:12725–12733.
23. Wang, Y., and E. Tajkhorshid. 2008. *Proc. Natl. Acad. Sci. USA* 105:9598–9603.
24. Johnston, J. M., S. Kahlid, and M. S. P. Sansom. 2008. *Mol. Mem. Biol.* 25:506–517.
25. Aksimentiev, A., and K. Schulten. 1995. *Biophys. J.* 88:3745–3761.
26. Gropp, T., N. Brustovetsky, M. Klingenberg, V. Müller, K. Fendler, and E. Bamberg. 1999. *Biophys. J.* 77:714–726.
27. Altschul, S. F., W. Gish, W. Miller, E. W. Myers,and D. J. Lipman. 1990. *J. Mol. Biol.* 215:403–410.
28. Wheeler, D. L., T. Barrett, D. A. Benson, S. H. Bryant, K. Canese, V. Chetvernin, D. M. Church, M. DiCuccio, R. Edgar, S. Federhen, L. Y. Geer, Y. Kapustin, O. Khovayko, D. Landsman, D. J. Lipman, T. L. Madden, D. R. Maglott, J. Ostell, V. Miller, K. D. Pruitt, G. D. Schuler, E. Sequeira, S. T. Sherry, K. Sirotkin, A. Souvorov, G. Starchenko, R. L. Tatusov, T. A. Tatusova, L. Wagner, and E. Yaschenkoet. 2006. *Nucleic Acids Res.* D5–D12.
29. Larkin, M. A., G. Blackshields, N. P. Brown, R. Chenna, P. A. McGettigan, H. McWilliam, P. Valentin, I. M. Wallace, A. Wilm, R. Lopez, J. D. Thompson, T. J. Gibson, and D. G. Higgins. 2007. *Bioinformatics* 23:2947–2948.
30. Thompson, J. D., D. G. Higgins, and T. J. Gibson. 1994. *Nucleic Acids Res.* 22:4673–4680.
31. Gouet, P., and X. Robert, and E. Courcelle. 2003. *Nucleic Acids Res.* 31:3320–3323.

GenInfo Identifier	Species	Isoform	GenInfo Identifier	Species	Isoform
gi|157127675	*Aedes aegypti*		gi|13775208	*Homo sapiens*	AAC4
gi|92090585	*Anopheles gambiae*	AAC1	gi|67083835	*Ixodes scapularis*	
gi|129563830	*Antechinus flavipes*	AAC1	gi|225713100	*Lepeophtheirus salmonis*	AAC1
gi|58531215	*Apis mellifera*		gi|6942136	*Lucilia cuprina*	
gi|19883932	*Arabidopsis thaliana*	AAC1	gi|28207648	*Manduca sexta*	
gi|4836655	*Ascaris suum*		gi|124295296	*Marsupenaeus japonicus*	
gi|156089447	*Babesia bovis*		gi|156481748	*Monochamus alternatus*	
gi|158631166	*Bombyx mori*		gi|148747424	*Mus musculus*	AAC1
gi|39654366	*Bos taurus*	AAC1	gi|22094075	*Mus musculus*	AAC2
gi|32189334	*Bos taurus*	AAC2	gi|30409998	*Mus musculus*	AAC4
gi|32189336	*Bos taurus*	AAC3	gi|89213828	*Myzus persicae*	
gi|114051019	*Bos taurus*	AAC4	gi|22506695	*Nyctotherus ovalis*	
gi|33391179	*Branchiostoma belcheri*		gi|221665139	*Oncorhynchus mykiss*	AAC2
gi|170590562	*Brugia malayi*		gi|154091018	*Oryctolagus cuniculus*	AAC2
gi|71991728	*Caenorhabditis elegans*	AAC1	gi|225708582	*Osmerus mordax*	AAC2
gi|66359700	*Cryptosporidium parvum*		gi|187936979	*Ovis aries*	AAC1
gi|170039111	*Culex quinquefasciatus*	AAC2	gi|187936981	*Ovis aries*	AAC2
gi|47550717	*Danio rerio*	AAC1	gi|187936983	*Ovis aries*	AAC3
gi|192453566	*Danio rerio*	AAC3	gi|113204648	*Pacifastacus leniusculus*	
gi|122938545	*Dendrolimus punctatus*		gi|467989	*Plasmodium falciparum*	
gi|66827623	*Dictyostelium discoideum*		gi|82539417	*Plasmodium yoelii*	
gi|254728	*Drosophila melanogaster*		gi|197098206	*Pongo abelii*	AAC2
gi|17737302	*Drosophila melanogaster*	AAC2	gi|4115750	*Rana rugosa*	
gi|2655147	*Drosophila pseudoobscura*		gi|4567152	*Rana sylvatica*	
gi|2655149	*Drosophila subobscura*		gi|38014819	*Rattus norvegicus*	AAC1
gi|157929872	*Epinephelus coioides*		gi|32189350	*Rattus norvegicus*	AAC2
gi|225717008	*Esox lucius*	AAC2	gi|209732444	*Salmo salar*	AAC2
gi|15559050	*Ethmostigmus rubripes*		gi|197260782	*Simulium vittatum*	
gi|22506699	*Euplotes sp.*		gi|47523888	*Sus scrofa*	AAC3
gi|57530120	*Gallus gallus*	AAC1	gi|122131406	*Tachyglossus aculeatus*	AAC2
gi|54020693	*Gallus gallus*	AAC3	gi|57506724	*Takifugu rubripes*	AAC1
gi|1197164	*Halocynthia roretzi*		gi|57506722	*Takifugu rubripes*	AAC3
gi|154091282	*Heliconius melpomene*		gi|71030136	*Theileria parva*	
gi|151384885	*Helicoverpa armigera*		gi|13445807	*Toxoplasma gondii*	
gi|55749577	*Homo sapiens*	AAC1	gi|150036382	*Trichostrongylus vitrinus*	
gi|62089230	*Homo sapiens*	AAC2	gi|148224610	*Xenopus laevis*	AAC2
gi|156071462	*Homo sapiens*	AAC3	gi|45360477	*Xenopus tropicalis*	AAC1

Table 3 Sequences used for the MSA. For each sequence the GenInfo Identifier, the species and if available the isoform is listed.

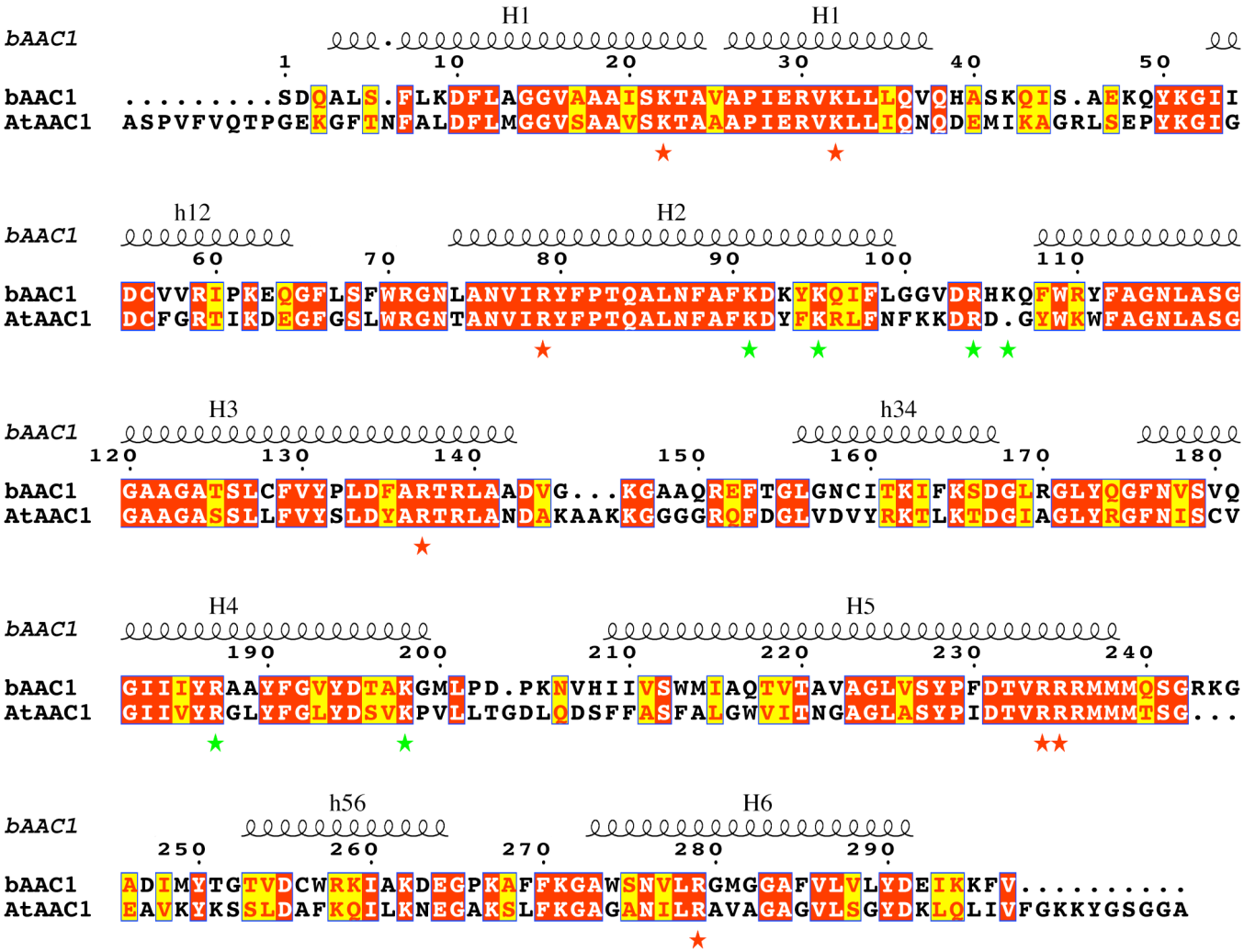

FIGURE 11 Sequence alignment of bAAC1 and AtAAC1. Secondary structure elements of bAAC1 (PDB structure 1OKC [11]) are indicated above. Basic residues of the upper patch (K91, K95, R104, R106, R187, K198) and of the lower patch (K22, K32, R79, R137, R234, R235, R279) are marked by green and red stars, respectively. Numbering is according to the sequence of bAAC1. The alignment was prepared with ClustalW [30] and rendered with ESPript [31].